RAM ROBOTICS AND MECHATRONICS

Development of a multi-rotor platform with integrated thrust sensors

J.L.J. (Jasper) Scholten

MSc Report

Committee:
Prof.dr.ir. S. Stramigioli
Dr.ir. T.J.A. de Vries
Dr.ir. M. Fumagalli
Prof.dr.ir. G.J.M. Krijnen

October 2014

Report nr. 023RAM2014
Robotics and Mechatronics
EE-Math-CS
University of Twente
P.O. Box 217
7500 AE Enschede
The Netherlands

UNIVERSITY OF TWENTE.

MIRA BIOMEDICAL TECHNOLOGY AND TECHNICAL MEDICINE

CTIT

Development of a multi-rotor platform with integrated thrust sensors

Jasper L.J. Scholten

Abstract— **The work presented in this paper focuses on the design and realization of a micro sized multi-rotor Unmanned Aerial Vehicle (UAV) with integrated thrust sensors. The goal has been to use the measured (actual) thrust in a feedback loop for thrust control for each motor and propeller, during flight. Furthermore, the aim has been to create a low-cost and easy to use multi-rotor research platform. The multi-rotor consists of a single printed circuit board, weighs approximately 99 grams (without battery) and measures 226 [mm] x 226 [mm] with propellers. Strain gauges positioned on the arms that connect the actuators to the base of the multi-rotor are used to measure the thrust. The UAV features a 10 degree of freedom Inertial Measurement Unit (IMU) and optionally the Gumstix Overo computer-on-module (RAMstix software compatible), together with its camera, the Caspa FS/VL. Because of its modular design, the multi-rotor can be extended by user designed modules and supports several communication modules with varying ranges (indoor [<100m], outdoor [>1km]), connection speeds (250kbps-2Mbps) and several standards (Bluetooth, WiFi). Proper functioning of the realized UAV has been shown by means of submodule tests. Further testing is needed, in which the usefulness of the thrust sensor should be demonstrated. One problem was surfaced though; the arms exhibit an unwanted torsional vibration that results in unreliable electrical connections.**

I. Introduction

In the last decade there has been an increasing interest in aerial robotics; especially in multi-rotor platforms, because of their simplicity of construction, their ability to hover and their ability to vertically takeoff and land (VTOL). The last few years, it has been possible to create smaller micro aerial robots with better performance and more advanced features. These small micro aerial robots have received great attention due to the favorable scaling laws; e.g. with respect to their agility [1] and due to their potential fields of application, such as swarm formations.

In [2], [1] and [3], micro-sized multi-rotors are presented that represent the current state-of-the-art. In [2], an 86g, 232 mm diameter open source micro UAV is created that is constructed on a single Printed Circuit Board (PCB). It has a 9 Degree of Freedom (DoF) Inertial Meaurement Unit (IMU) and a Gumstix Overo [ref:gumstix] compute-on-module that is able to run the Robot Operating System (ROS). In [1], a 73g, 210 mm diameter micro quad-rotor is presented that is able, due to its agility, to operate in a team of 20 micro quad-rotors in swarm formations. In [3], a 128g, 260 mm diameter quad-rotor is developed with an on-board FPGA for image processing, giving it the possibility to perform visual feature detection of the ground and as a result, operate autonomously.

The dynamics of multi-rotors have been researched profoundly in the last decade; e.g. [4], [5]. To control the motors of a multi-rotor, often a static relationship between the actuator's speed and the thrust generated is assumed [4]. Given the desired thrust, the required angular velocity of the rotor is computed, which is then used by a speed controller to control the rotor's speed. This scheme however has problems in dealing with aerodynamic effects, such as the ground effect [6] or wind disturbances that are either not rejected by the control law [7] or require a sophisticated control law [8], [9], [10].

In [11], an adaptive Luenberger observer is used to estimate the thrust of each individual actuator. A hardware-in-the-loop simulation, consisting of a 1 degree of freedom system, has been preformed to validate the presented observer. However, it is based on a linear model that neglects nonlinear cross coupling terms and therefore only applicable to near hover operations.

In [12], estimates of both the rotor's speed and motor current are used to estimate and control the aerodynamic power. Although regulating aerodynamic power is not the same as controlling the actual thrust, the algorithm is shown to be more robust against aerodynamic effects such as axial and horizontal airflow disturbances. As a result, it outperforms current state-of-the-art motor controllers that control the rotor's angular velocity, but hasn't been implemented and tested on a flying UAV.

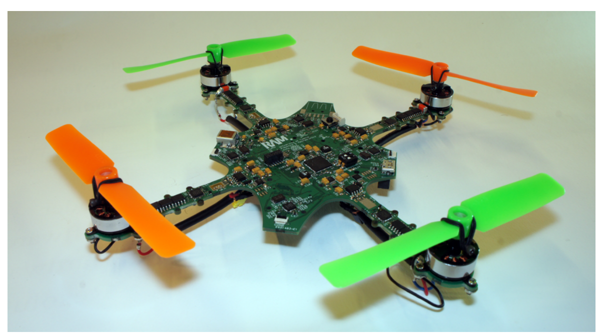

Fig. 1. Designed multi-rotor with integrated thrust sensors.

This paper proposes a novel scheme where, instead of a model based thrust estimation approach, an attempt is made to control the actual thrust of each actuator by use of integrated thrust sensors. In this first step, a new micro UAV multi-rotor has been designed (Figure 1) to incorporate thrust sensors while also providing an new agile research platform. The UAV is made out of a single printed circuit board that simplifies its design and fabrication. Furthermore, it facilitates the integration of thrust sensors.

This paper is organized as follows: in Section II, the novelty is analysed and the performance determining parameters are identified. In Section III, the design of the multi-rotor is presented, after which in Section IV the control scheme is discussed. In Section V, the experiments performed and the results obtained are presented. Finally in Section VI a conclusion is drawn and recommendations are made.

II. Analysis

In order to measure the thrust, the idea is to integrate thrust sensors, in the form of strain gauges, in the arms of the multi-rotor as illustrated in Fig. 3. The thrust generated by each actuator creates a moment of force at each point located on the arm. Once a specific point is chosen, due to bending, a strain occurs which can be measured and interpreted as a stress depending on the mechanical properties of the arm. Under the assumption that a homogeneous linear elastic material is used in its stress range, Hooke's law is valid and the strain is proportional to the stress at the point of interest. It is this strain that can be measured by means of strain gauges (as the name suggests). As a result, implementing strain gauges on the arms of a multi-rotor enables the measurement of the thrust forces:

$$\epsilon = \frac{L \cdot d}{I \cdot E} \cdot F_T \text{ (refer to Fig. 2)} \tag{1}$$

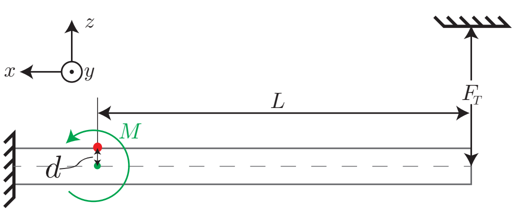

Fig. 2. Illustration of strain measurement where M is the moment of force created by the force F_T and arm L.

where ϵ is the strain, F_T the thrust, L the length of the arm, d the distance between the location of the strain gauge and the arm's neutral axis, I the area moment of inertia and E the Young's modulus of the material.

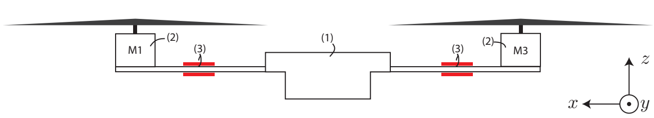

Fig. 3. Cross section of a multi-rotor. With (1), the integrated electronics and battery, (2) the motors and their corresponding propellers, (3) the integrated strain gauges used to measure the thrust.

However, a multi-rotor is best viewed as a floating mechanical system; in other words, it has no connection with the fixed world. Due to the fact that several sources of force are present, the strain measured by each strain gauge is not only due to the corresponding actuator's thrust. To further analyse this, a simple model, represented by the iconic diagram in Fig. 4, is created. This model is analysed in Section II-A. In Section II-B it is determined whether thrust control can be achieved and in Section II-B.3 insight is gained in the performance limitations.

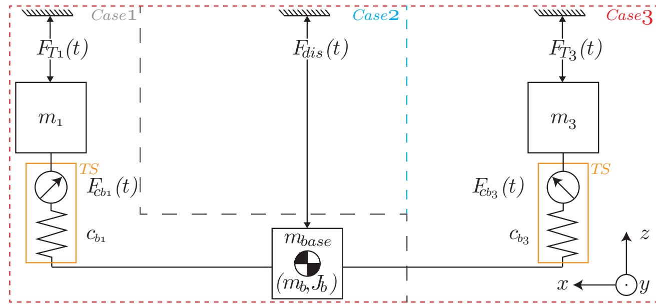

Fig. 4. A 1D model of a multi-rotor's cross section. Case $\{1, 2, 3\}$ represent the cases that will be analysed while TS represent the Thrust Sensor.

The following notation is used throughout this analysis: H_A^B denotes the transfer function from A to B, F_{Tx} denotes the (thrust) force of actuator x and $F_{c_{by}}$ denotes the force between the base of the multi-rotor and actuator y. Furthermore, most equations are linear and written in Laplace domain and therefore, where possible, (s) is omitted.

The following coordinate definition is used (refer to Fig. 5): the x-axis of the multi-rotor is aligned with actuator 1 and 3 and points from the center of the PCB towards motor 1, while the y-axis is aligned with actuator 2 and 4 and points to motor 2. τ_x denotes the torque about the x-axis and is created by actuator 2 and 4. τ_y denotes the torque about the y-axis and is created by actuator 1 and 3. τ_z is the torque about the z-axis and is created by all four actuators. The rotation direction of the first and third motor are opposite to the rotation direction of the second and fourth motor and hence always have a negative magnitude. Therefore τ_1 and τ_3 are likewise negative in magnitude and as a result, t_z can be controlled in both directions.

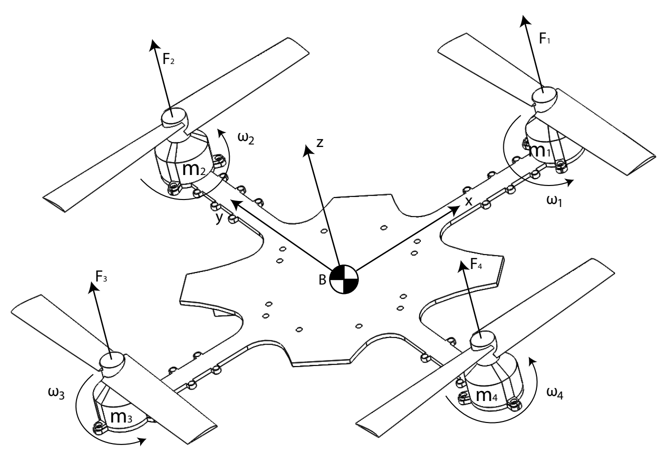

Fig. 5. Illustration of the multi-rotor's body fixed frame, thrust and angular velocities.

A. Model analysis

In Fig. 4 the mass m_1 and m_3 represent the mass of actuator 1 (motor + propeller) respectively actuator 3. The mass of the base of the multi-rotor is represented by m_{base} and this mass includes its inertia. Furthermore, the following assumptions are applicable:

1) The actuators and base of the multi-rotor are rigid.
2) The operating regime of the arms is such that Hooke's Law is valid at all times.
3) Each thrust sensor (TS), i.e. arm with strain gauge, is modeled as an ideal force sensor, measuring $F_{c_{by}}(t)$, in series with an ideal spring. The corresponding spring constant being c_{by}. The spring represents the (bending) stiffness of the arm in the operating area defined in item 2. In general the damping does not dominate the dynamics of the mechanism and will only complicate the considerations that follow. Therefore, the damping is neglected.
4) The forces acting on the multi-rotor are the thrust forces F_{Tx} on the actuators and a disturbances force $F_{dis}(t)$ on the base of the multi-rotor. The forces include all aerodynamic effects and hence represents the total aerodynamic force.

The following three cases are now analysed:

1) One actuator without disturbance force (c_{b3} is decoupled and F_{dis} remains zero).
2) One actuator with disturbance force (c_{b3} is decoupled).
3) Two(+) actuators with disturbance force.

Case 1) One actuator without disturbance force: In [13], classes of electromechanical motion systems are introduced for fourth-order mechanisms. The system in this first case, a mass-spring-mass plant of the fourth-order, corresponds to a flexible mechanism. Once the location of the actuator and sensor are chosen, the plant's transfer function can be derived. The denominator polynomial of the plant's transfer function is independent on the location of the actuator and sensor. The numerator polynomial however does depend on the location of the actuator and sensor.

In motion control applications, as considered in [13] the goal is to control the displacement or velocity of the end-effector. Therefore, the focus lies on the open loop transfer function from the actuator's force $F_{T1}(t)$ to the displacement or velocity of the mass whose position or velocity is measured. However, in this case the goal is to control the thrust force and hence, the focus lies on the open loop transfer function from the actuator's force $F_{T1}(t)$ to the force exerted on the base of the multi-rotor ($F_{c_{b1}}$).

Due to the location of actuator F_{T1} and sensor $F_{c_{b1}}$, the following open-loop transfer function is derived:

$$F_{c_{b1}} = H_{F_{T1}}^{c_{b1}} \cdot F_{T1} \tag{2}$$

with:

$$H_{F_{T1}}^{c_{b1}} = \frac{\frac{c_{b1}}{m_1}}{s^2 + \frac{c_{b1}}{m_1} + \frac{c_{b1}}{m_b}} = \frac{\omega_{ar,m_1}^2}{s^2 + \omega_r^2} \tag{3}$$

$$\omega_r = \sqrt{\frac{c_{b1}}{m_{base}} + \frac{c_{b1}}{m_1}} \tag{4}$$

$$\omega_{ar,m_1} = \sqrt{\frac{c_{b1}}{m_1}} \tag{5}$$

Equation 3 can be characterised as a standard second order low pass transfer function with two poles ($\pm\omega_r i$) located on the imaginary axis in the pole-zero map. These poles determine the bandwidth of the system (eq. 4) and introduce a total phase shift of $-\pi$. Even though no anti-resonance frequency is present, $\frac{c_{b1}}{m_1}$ does represents a time constant in the numerator and therefore is represented by $\omega_{ar,m1}$. For low frequencies equation 3 converges to:

$$H_{F_{T1}}^{c_{b1}}(0) = \frac{\omega_{ar,m_1}^2}{\omega_r^2} \tag{6}$$

The maximum achievable gain is unity and therefore the highest measurement sensitivity within the bandwidth of the system is achieved when:

$$|F_{c_{b1}}(j\omega)| = |F_{T1}(j\omega)| \ \forall\omega \in [0, \omega_{BW}) \tag{7}$$

The bandwidth of the system (ω_{BW}) in case no damping is present is defined as ω_r.

Case 2) One actuator with a disturbance force: In this second case a disturbance force is added to the system. By use of the superposition principle, the force measured by the force sensor can be described by equations 3, 8, 9 and 10.

$$F_{c_{b1}} = H_{F_{T1}}^{c_{b1}} \cdot F_{T1} - H_{dis}^{c_{b1}} \cdot F_{dis} \tag{8}$$

$$H_{dis}^{c_{b1}} = \frac{\frac{c_{b1}}{m_b}}{s^2 + \frac{c_{b1}}{m_1} + \frac{c_{b1}}{m_b}} = \frac{\omega_{ar,m_b}^2}{s^2 + \omega_r^2} \tag{9}$$

$$\omega_{ar,m_b} = \sqrt{\frac{c_{b1}}{m_b}} \tag{10}$$

As mentioned, the only difference between the open loop transfer functions, $H_{dis}^{c_{b1}}$ and $H_{F_{T1}}^{c_{b1}}$, is the numerator: ω_{ar,m_1}^2 versus ω_{ar,m_b}^2. The denominator of the plant's transfer function and therefore, the bandwidth and resonance frequency remain the same. As a result, only the steady state gain of both open loop transfer functions differ. For most multi-rotors, the mass of the actuator is smaller than the mass of its base, and thus the disturbance force is attenuated with a higher degree than the thrust force:

$$|H_{dis}^{c_{b1}}(j\omega)| < |H_{F_{T1}}^{c_{b1}}(j\omega)| \ \forall\omega \tag{11}$$

Case 3) Two(+) actuators with disturbance force: In this last case a second actuator is added to the system. The open loop transfer function is still rather simple to express, especially when taken into account the system has a symmetry:

$$H_{dis}^{c_{b1}} = H_{dis}^{c_{b3}} = H_{dis}^{c} \tag{12}$$

$$H_{F_{T1}}^{c_{b1}} = H_{F_{T3}}^{c_{b3}} = H_{F_T}^{c} \tag{13}$$

yielding in terms of sensitivity:

$$F_{c_{b\{1,3\}}} = S_{F_{T\{1,3\}}} \cdot F_{T\{1,3\}} - S_{F_{dis}} \cdot F_{dis} - S_{F_{T\{3,1\}}} \cdot F_{T\{3,1\}} \tag{14}$$

$$S_{F_{T\{1,3\}}} = \frac{H_{F_T}^{c}}{1-(H_{dis}^{c})^2} \tag{15}$$

$$S_{F_{dis}} = \frac{H_{dis}^{c} - (H_{dis}^{c})^2}{1-(H_{dis}^{c})^2} \tag{16}$$

$$S_{F_{T\{3,1\}}} = \frac{H_{dis}^{c} \cdot H_{c}^{dis} \cdot H_{F_T}^{c}}{1-(H_{dis}^{c})^2} \tag{17}$$

$$H_{c}^{dis} = 1 \tag{18}$$

For the complete derivation please refer to Appendix I.

With respect to the second case, the second actuator increases the steady state gain of both sensitivity functions $S_{F_{T\{1,3\}}}$ and $S_{F_{dis}}$. Furthermore a dependency on the thrust force of the second actuator, F_{T3}, is introduced.

From (3), (9) and (19) it can be deduced that for low frequencies, i.e. $\omega \ll \omega_{\{ar,r\}}$, the following holds:

$$\begin{aligned} |S_{F_{T\{1,3\}}}(j\omega)| &= |1 - S_{F_{dis}}(j\omega)| \\ &= |1 - S_{F_{T\{3,1\}}}(j\omega)| \end{aligned} \tag{19}$$

Symbolic analysis has shown that the measured force for a multi-rotor with four actuators equals:

$$F_{c_{by}} = S_{F_{Ty}}^{y} \cdot F_{Ty} - S_{dis}^{y} \cdot (F_{dis} + \sum_{i \neq y} F_{Ti}) \tag{20}$$

For a multi-rotor with four actuators equation 19 remains valid and is not influenced by mass variations of the actuators and stiffness variations of the multi-rotor's arms. However, variations do result in the introduction of more resonance and anti-resonance frequencies. As a rule of thumb, the lowest (anti-)resonance frequency can be approximated by the combination of arm and actuator that lead to the lowest (anti-)resonance frequency. For the complete derivation refer to Appendix I-B.

B. Thrust control

In order to evaluate whether thrust control can be achieved, it has to be determined what the inputs of a multi-rotor are and how these are being controlled. For a multi-rotor with four actuators four degrees of freedom can be controlled namely, three rotational DoFs and one translational DoF: the (vertical) translation in its z-axis. In order to control these four DoFs the actuator's thrust force has to be mapped to the total thrust force and torque about each axis (refer to Fig: 5):

$$\begin{bmatrix} F_z \\ \tau_x \\ \tau_y \\ \tau_z \end{bmatrix} = \begin{bmatrix} 1 & 1 & 1 & 1 \\ 0 & d_{arm} & 0 & -d_{arm} \\ d_{arm} & 0 & -d_{arm} & 0 \\ -k & k & -k & k \end{bmatrix} \cdot \begin{bmatrix} F_{c_{b1}} \\ F_{c_{b2}} \\ F_{c_{b3}} \\ F_{c_{b4}} \end{bmatrix} \tag{21}$$

Here d_{arm} denotes the distance between the actuator and the multi-rotor origins. k denotes the thrust to torque coefficient of the actuator and is often empirically determined. These desired thrust forces are now in general converted by a static relationship to an angular velocity. This angular velocity is then used to control the speed of the actuator in a closed loop.

In case a feedback loop around the measured force is formed, a mapping is required from the thrust force and torques to the measured force $F_{c_{by}}$. As the measured forces do not only depend on F_{Ty} it has to be determined if and how the thrust force and torques can be mapped to the measured forces. Furthermore, if a mapping exists, it has to be determined what the limitations are and how these can be influenced.

At first, for both the thrust force and torques it is determined if they can be mapped, after which the limitations are determined.

1) Thrust force: In section II-A it has been shown that the measured forces depend on both the disturbance force and all thrust forces. The translational dynamics of a multi-rotor with four actuators, expressed in its body fixed frame, can be expressed as:

$$m_{base} \cdot \dot{v}_b^{b,0} = \sum_{y=1}^{4} F_{c_{by}} + F_{dis} \tag{22}$$

Here $v_b^{b,0}$ represents the velocity of the multi-rotor's base (b) with respect to the inertial frame of reference (0) and expressed in the multi-rotor's body fixed frame (b).

In the absence of a disturbance force, by controlling $F_{c_{by}}$ the total thrust force can be controlled. In case a disturbance force is present and the measured force is regulated, any error in the state of the multi-rotor is caused by the disturbance force. Moreover, as the measured force depends on the disturbance force, a part of the disturbance force is rejected by closing the loop around the measured force $F_{c_{by}}$.

2) Torques: In order to determine the torques about the x and y-axis of the multi-rotor, knowledge of the actual actuators their forces (F_{Tx}) and the distances between the actuators and the multi-rotor's origin are required. In this case, a measurement is available ($F_{c_{by}}$) in which F_{Ty} is reflected, but it does not only contain F_{Ty}. However, as each force on the multi-rotor is reflected in each measurement, it is expected that the measured forces can be mapped to the torques in the same manner and therefore the following is tried:

$$\tau_x = d_{arm} \cdot (F_{T2} - F_{T4}), \text{ try:}$$
$$\tau_x = d_{arm} \cdot (F_{c_{b2}} - F_{c_{b4}})$$

Using equation (20) this yields:

$$\tau_x = d_{arm} \cdot \Big((S^1_{F_{T1}} + S^3_{dis}) \cdot F_{T1} - (S^3_{F_{T3}} + S^1_{dis}) \cdot F_{T3} - (S^1_{dis} - S^3_{dis}) \sum_{i=2,4,dis} F_{Ti} \Big) \tag{23}$$

In case the arms and actuators are well matched, i.e. equations 12 and 13 are valid, S^1_{dis} becomes equal to S^3_{dis} and thus the disturbance forces cancel out. Furthermore $S^1_{F_{T3}}$ becomes equal to $S^3_{F_{T3}}$ and as a result, the following is deduced:

$$\tau_{m\{x,y\}} = \frac{\omega^2_{r,m_{act}}}{s^2 + \omega^2_{r,m_{act}}} \cdot \tau_{\{x,y\}} \tag{24}$$

$$\omega_{r,m_{act}} = \sqrt{\frac{c}{m_{act}}} \tag{25}$$

and for the torque about the z-axis:

$$\tau_{mz} = \frac{\omega^2_{r,m_{act}}}{s^2 + \omega^2_{r,m_{act}}} \cdot \tau_z \tag{26}$$

In other words, in case equations 12 and 13 are valid, all torques acting on the multi-rotor can be measured within the bandwidth of the system. As a result the desired torques can be mapped to the measured forces $F_{c_{by}}$.

3) Limitations: More insight in the proposed scheme is required to determine its limitation as in reality the actuators will vary in mass as does the stiffness of the arms. By introduction of the following mass ratio, the limitations can be expressed more clearly.

$$R_m = \frac{m_{base}}{m_{act}} \tag{27}$$

with m_{act} being the average mass of the actuators.

The influences of mass variations of the actuators can be determined by defining the mass of the actuators as follows:

$$m_{\{1,2,3,4\}} = m_{act} \cdot (1 + X_{\{1,2,3,4\}}) \tag{28}$$

where $X_{\{1,2,3,4\}}$ is the deviation of each actuator with respect to the average actuator's mass.

Now the measured thrust force for a multi-rotor with four actuators can be expressed for low frequencies, i.e. $\omega \ll \omega_{\{ar,r\}}$, as (refer to equation 20 and Appendix I-B):

$$F_{c_{bx}}(0) = \frac{3 + R_m + \sum_{i \neq x} X_i}{4 + R_m + \sum_{i=1}^4 X_i} \cdot F_{Tx}(0) - \sum_{i \neq x} \frac{1 + X_x}{4 + R_m} \cdot F_{Ti}(0) - \frac{1 + X_x}{4 + R_m} \cdot F_{dis}(0) \tag{29}$$

$$F_{c_{bx}}(0) = \frac{3 + R_m}{4 + R_m} \cdot F_{Tx}(0) - \sum_{i \neq x} \frac{1}{4 + R_m} \cdot F_{Ti}(0) - \frac{1}{4 + R_m} \cdot F_{dis}(0) \tag{30}$$

As the stiffness constants are not present in equation (30) stiffness variations of the multi-rotor's arm do not influence the measured force. Variations in the actuator's mass do influence the measurement, but do not impact the performance of a closed loop thrust controller as the loop is closed around the measured force. The achievable bandwidth is determined by the anti-resonance and resonance frequencies present. These frequencies should be obtained from numerical analysis or simulation but, in case the mass and stiffness of each arm and actuator is well matched, i.e. no mass/stiffness variations, $H^{c_{by}}_{F_{Ty}}$ equals:

$$H^{c_{by}}_{F_{Ty}} = \frac{\omega_{r,m_y}}{s^2 + \omega_{r,m_y}} \cdot \frac{3 \cdot c + R_m \cdot c + R_m \cdot m \cdot s^2}{4 \cdot c + R_m \cdot c + R_m \cdot m \cdot s^2} \tag{31}$$

Hence the lowest resonance frequencies is ω_{r,m_y}. In case of mass or stiffness variations, as a rule of thumb, the lowest frequency can be approximated by the combination of actuator's mass and stiffness that lead to the lowest frequency.

With the introduction of the mass ratio and the definition of the actuator's mass, the error in the torque measurement for low frequencies, i.e. $\omega \ll \omega_{\{ar,r\}}$, can be expressed as (refer to equation 23 and Appendix I-B):

$$\begin{aligned}\tau_{e\{x,y\}}(0) = {} & (1 - \frac{4 + R_m + X_2 + X_4}{4 + R_m + \sum_{i=1}^4 X_i}) \cdot \tau_{\{x,y\}}(0) + \\ & (\frac{2 \cdot X_{\{3,4\}}}{4 + R_m + \sum_{i=1}^4 X_i}) \cdot F_{T\{1,2\}}(0) - \\ & (\frac{2 \cdot X_{\{1,2\}}}{4 + R_m + \sum_{i=1}^4 X_i}) \cdot F_{T\{3,4\}}(0) - \\ & \sum_{i=\{2,1\},\{4,3\},dis} (\frac{X_{\{3,4\}} - X_{\{1,2\}}}{4 + R_m + \sum_{i=1}^4 X_i}) \cdot F_i\end{aligned} \tag{32}$$

It can be concluded that a variation of the actuator mass of 10% together with a mass ratio of 10 creates an uncertainty of 2.9 % plus an additional torque error of $1.45\% \cdot |\tau_{\{x,y\}}(0)|$. Furthermore 1.45% of the disturbance force and the other actuator's thrust forces are measured. These errors will result in inaccuracy of the torque to force mapping.

In order to reduce this error an high mass ratio is required. In case the mass ratio converges to infinity the measured force converges to:

$$\lim_{Rm\to\infty} F_{c_{by}} = \frac{\omega_{r,m_y}}{s^2 + \omega_{r,m_y}} \cdot F_{Ty} \tag{33}$$

And hence the torque converges to:

$$\lim_{Rm\to\infty} \tau_{m\{x,y\}} = \frac{\omega_{r,m_{\{2,1\}}}}{s^2 + \omega_{r,m_{\{2,1\}}}} \cdot F_{T\{2,1\}} - \tag{34}$$

$$\frac{\omega_{r,m_{\{4,3\}}}}{s^2 + \omega_{r,m_{\{4,3\}}}} \cdot F_{T\{4,3\}} \tag{35}$$

The dependency on the disturbance force has been eliminated and for low frequencies, i.e. $\omega \ll \omega_{ar,r}$, the error converges to zero.

Finally, it can be concluded that for torque measurement a high mass ratio is desired while for the thrust force a trade-off is formed. This is, because for the thrust force measurement to be insensitive to the disturbance force an high mass ratio is required. This enables, in case the state of multi-rotor is known, to determine the disturbance force. On the other hand, a low mass ratio enables better control of the total thrust force as a larger part of the disturbance force is reflected in the measurements and therefore can be rejected. As for the torque measurements, a low mass ratio increases the error in the mapping significantly and therefore an high mass ratio is required. Furthermore, the measured torque, in case the desired accuracy can be met, can be used to improve the attitude estimation and hereby further improve the performance; again stressing the importance of an high mass ratio.

III. Multi-rotor Design

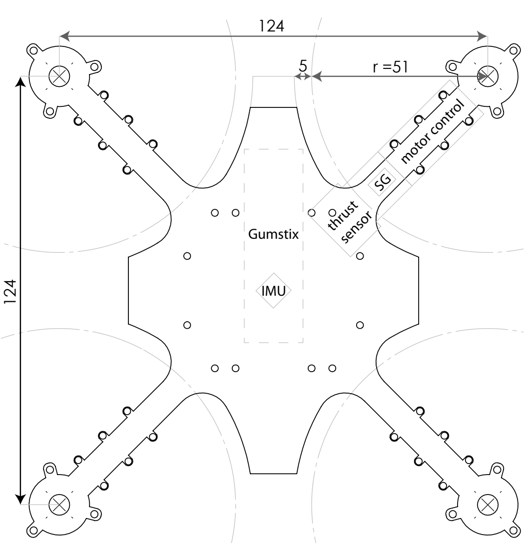

Fig. 6. Design of the multi-rotor with integrated thrust sensors. For one arm the position of the motor controller and thrust sensor is drawn. The Gumstix Overo, outlined with dash lines, is located at the bottom side of the multi-rotor. 5 [mm] of spacing is used between the propeller and the base of the multi-rotor to minimize the disturbance of the airflow.

In [14], a preliminary multi-rotor design has been made which is based on user requirements [15] and experimental results of the available combinations of micro-sized motors and propellers. Given these results, the designed multi-rotor uses 4" inch (101.6 mm) propellers. Together with the main user requirements of an optional Gumstix with camera(s) and preferable high mass ratio, this has led to the design of the multi-rotor's main board as shown in Fig. 6.

In total, the multi-rotor electronics consist of two 6-layers printed circuit boards; the main board and a power supply board. The main board forms the frame of the multi-rotor and houses all the electronics except the power supply electronics; these are located on the power supply board. This power supply board distributes power to the subsystems, including the actuators, and is to be attached to the bottom of the main board.

The overall dimensions of the multi-rotor are 226 [mm] by 226 [mm] and it weighs 99 grams. This is without battery and additional modules attached. The mass ratio, as introduced in the analysis, depends on the battery used and with either an 1800mAh 11.1V battery or an 950mAh 11.1V battery, the mass ratio equals 5.1 respectively 3.7. The corresponding hover time equals (theoretically) 26 minutes respectively 20 minutes and a thrust to mass ratio of 2.3 respectively 3.3 is obtained.

For a mass ratio of 5.1 a mass variation of 10% will now, in theory, result in an error in the torque measurement of 4.5% plus a maximum of 2.25 % of the actual torque and disturbance force is measured. This holds for frequencies lower than the lowest resonance frequency present. The lowest resonance frequency, formed by the stiffness of the arm and mass of the actuator, is approximated to be equal to 50 Hz. This frequency can however, in case experiments deem this necessary, be increased by adding external support to stiffen the arm section holding the motor controller and motor. This support can be mounted to the six mounting holes that are located on the arms as shown in Fig. 6.

The thrust sensors, in the form of (semiconductor) strain gauges, are located on pads on both the top and bottom side of the arms (SG in 6). As they are placed in a half-bridge configuration, the measurement is insensitive to changes in the temperature. Furthermore, as they are placed in the center of the arm's longest axis, i.e. aligned with the multi-rotor's x and y axis, axial strain is rejected.

For future research projects it is possible to add additional modules via the corresponding mounting holes and electronic headers, including USB peripherals. This gives the user the option to attach modules like a GPS module, cameras, ultrasound altitude sensors etcetera.

In the next section a systematic overview of the system is presented and its main parts are discussed shortly.

A. System overview

In Fig. 7 a systematic overview of the multi-rotor is shown with all its subcomponents and connections.

The hart of the multi-rotor is the Low Level Controller (LLC) that communicates with the user via an external RF communication module, computes the attitude and altitude based on the measurements of the sensors and communicates

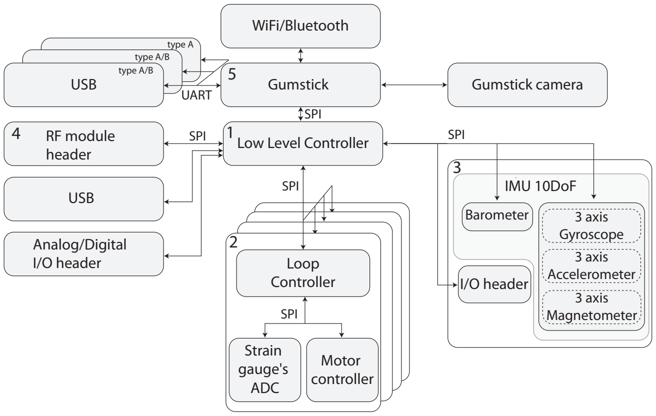

Fig. 7. Designed multi-rotor with integrated thrust sensors.

with the loop controllers that control the motor controllers. Each main subcomponent, numbered in Fig. 7, is discussed below.

1) LLC: the low lever controller is a 8/16-bit RISC based microcontroller running at 32 MHz (AtXmega128A3U). It has, among other features, multiple SPI interfaces, an event and Direct Memory Access (DMA) controller and a full-speed USB interface. Each peripheral that requires direct communication with the LLC has been assigned a dedicated SPI interface. Furthermore all SPI interfaces can make use of the event and DMA controller; this increases the communication speed by offloading the CPU. The event system furthermore facilitates real-time performance, which can be crucial during complex flight maneuvers. The USB interface can be used, together with a boot-loader, to program the microcontroller and for debugging purposes. The choice for the XmegaAVR series has been made because users familiar with either the AVR series from Atmel or with an Atmel based Arduino should find the switch to the XmegaAVR series rather painless compared to switching to an ARM-based microcontroller.
2) a) LC: the loop controller is a 8-bit RISC based microcontroller running at 16MHz (Atmega88PA). Its main task is to control the speed of the motor. The speed reference is received from the LLC and the actual speed from the motor controller (MC). Its output is a Pulse Width Modulation (PWM) duty cycle which is sent to the motor controller via its second SPI interface. Its second task is to acquire the Analog Digital Converter's (ADC) result of the strain gauge measurement and eventually control the (thrust) force in a feedback loop.
   b) MC: the motor controller is also an 8-bit RISC based microcontroller running at 16MHz, but from the tinyAVR series (ATtiny861). It features an on board PLL oscillator that is able to create a fast peripheral clock of 64MHz. This clock is used to create three 10 bits PWM signal with a modulation frequency of 20kHz. These PWM signals are used to control the motors. The main task of the motor controller is to start the motor and keep the motor running with the desired PWM duty cycle. Due to the control being sensorless, this task uses most of the CPU's time, which is why the LC has been introduced.
3) The multi-rotor currently houses two sensor devices, one barometer and one 9-axis motion sensor, which together form the 10 Degree of Freedom Inertial Measurement Unit of the multi-rotor. The 9-axis motion sensor (MPU9250) includes an 3-axis accelerometer, a 3-axis gyroscope and a 3-axis magnetometer all in one single package. The accelerometer and magnetometer enable the determination of the absolute attitude while the gyroscope enables the determination of faster motions. Via a single SPI interface (or I2C) the data of all three internal sensors can be acquired. The barometer (MS5607-02BA03), accessible via SPI, enables the multi-rotor's altitude to be determined with a resolution of 20[cm].
4) For communication with the user, an RF module can be attached to the multi-rotor. Currently, a 2.4GHz module (nRF24L01+) is used which supports communication speeds up to 2 Mbps with an indoor range of roughly 30 meters. Due to the modular design, other communication modules (e.g. nRF905) that utilize lower frequencies (e.g. [433/868/915MHz]) can be used to extend the range, at the cost of data throughput.
5) For use with more sophisticated control algorithms or Digital Signal Processing (DSP), a Gumstix Overo and its camera can be fitted to the multi-rotor. The mounting holes gives the user the ability to design custom brackets for Gumstix's WiFi/Bluetooth antennas and camera(s).

IV. Control

The introduction of a closed loop thrust controller increases the number of cascaded controllers. As a result, the control structure of a UAV consist of three cascaded control loops as is shown in Figure 8. Note that often, an additional position loop is present and thus four cascaded control loops are formed. In order for a cascaded controller to outperform a single controller, the loop rate of the inner controller has to be higher than the outer controller, preferably by a factor 10. In order to facilitate this control scheme, the following loop rates are implemented:

- Speed control: 10 kHz
- Thrust control: 2 kHz (not yet implemented, but supported)
- Attitude control: 200 Hz

The loop rate should preferably be a factor 10 higher than the bandwidth of the system and therefore, a 20 Hz attitude bandwidth is possible. This bandwidth allows a multi-rotor to make acrobatic maneuvers in case the actuators have the required bandwidth. For the design multi-rotor a flip for example, in case a skew sine path is used with a PD

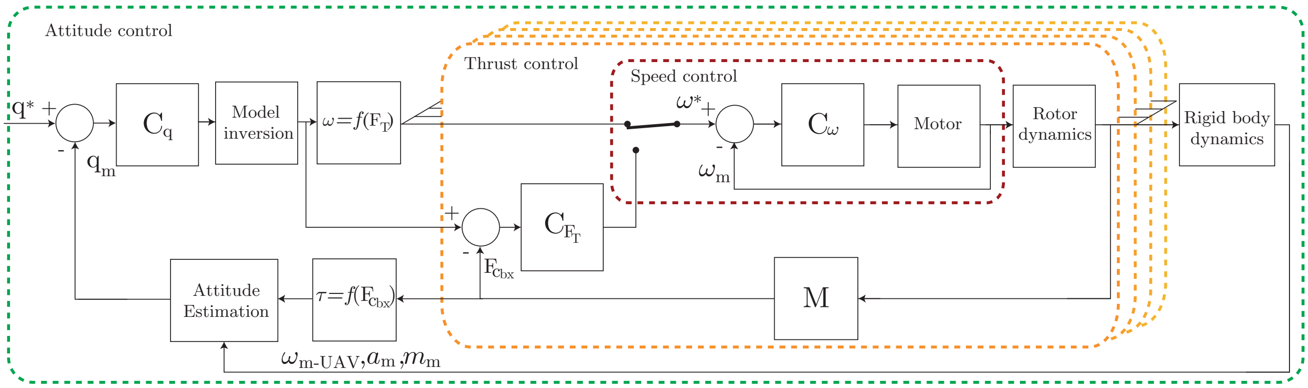

Fig. 8. Overview of the control structure of the multi-rotor.

controller, can be performed in 0.4 seconds with a tracking error of 2.9 degrees according to motion control theorems [13].

A. *Attitude estimation and control*

The attitude of the multi-rotor is currently estimated by use of the accelerometer, gyroscope and magnetometer. The data of these sensors is presented in the sensor's body fixed frame and hence can be used to estimate the attitude of the multi-rotor in its body fixed frame. A complementary filter, which is less computational intensive than a conventional Kalman-based algorithm and has the same performance, is used to estimate the attitude in quaternion representation [16]. The advantage of the quaternion representation is that no singularities are present and only four values are required to represent that attitude of the multi-rotor [17].

Currently, after computation of the error quaternion, the simplest approach is taken to control the multi-rotor in near hover conditions. Although this approach is not singularity free, no singularities will be present as it is only being used for near hover conditions. This approach consist of mapping the error quaternion to yaw (z-axis), roll (x-axis) and pitch (y-axis) Euler angels. A PD controller is implemented on each axis to control the corresponding angles and hence C_q (Fig. 8) consist of three PD controller. The PD controllers make use of the measured angular velocity of the gyroscopes (D-action) and the error angle (P-action). The gains have been tuned empirically.

V. Experimental validation

The following experiments have been performed:

1) Calibration of thrust sensor by using a sinusoidal speed reference.
2) Research of the influence of the ground effect on the thrust measurements.
3) Research of the influence of a wall on the thrust measurements.

Furthermore all the subsystems of the multi-rotor have been successfully tested. The communication between the subsystems also work reliably. However, due to torsional vibration of the arms, which are induced by the motors, several electrical connections on the arms have proved to be unreliable during take-off. As a result, the multi-rotor has yet to make its first flight and therefore only the mentioned experiments have been performed.

The setup for the performed experiments are discussed in Section V-A, after which the results are discussed in Section V-B. The results are evaluated in Section V-C.

A. *Experimental setup*

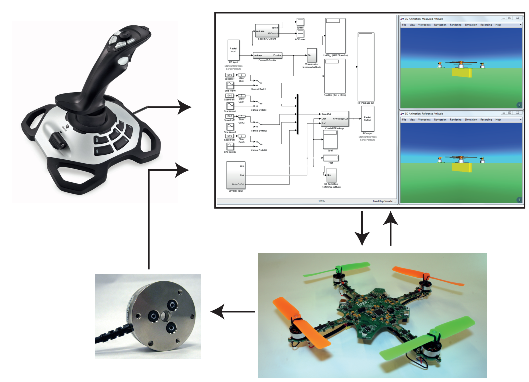

Fig. 9. Overview of the experimental setup

An overview of the test setup is given in Fig. 9. The experimental setup consist of the following modules:

1) The designed multi-rotor as described in Section III. The strain gauge's signal is sampled at 2 kHz. A second order IIR filter is applied with a cut of frequency of 200 Hz.
2) F/T Sensor [18]: A six-axis force and torque sensor which is being used to calibrate and serve as reference for the thrust measurements. The sensor is mounted on a table and attached, via a bracket, to the multi-rotor's base.
3) Ground station: the ground station consist of a PC running Simulink in real-time-windows-target mode. The PC communicates with the multi-rotor via a 2.4GHz communication module that is attached via USB. At a rate of 200 Hz, commands such as set points, are

being sent to the multi-rotor. After transmission of a acknowledged packet, the multi-rotor replies by sending a package. This package contains (desired) data that can be logged during the experiments. The ground station can also be interfaced with a joystick to generate the reference attitude. Both the measured attitude by the multi-rotor and the reference attitude can be displayed by use of Simulink's 3D animation toolbox. This way, the quaternions can be represented in a simple and intuitive way.

B. Results

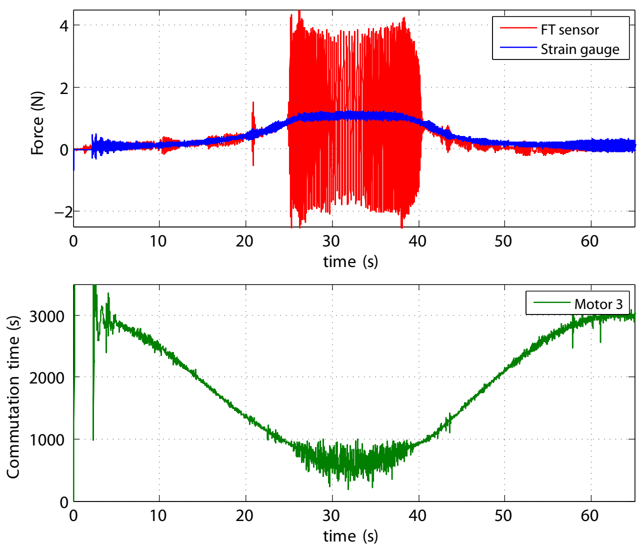

Fig. 10. Experiments 1: calibration measurement of the strain gauge located on the third arm. In the top plot the force measured by the strain gauge (blue) and the force measured by the F/T sensor (red) are shown. In the bottom plot the commutation time of the motor is shown which is inversely proportional to its speed.

In the top plot of Fig. 10 the force measured by the calibrated strain gauge and F/T sensor are shown. In the bottom plot the commutation time is shown. The commutation time is the time between two commutations of the brushless motor. This time is being measured by the speed controller and is inversely proportional to the speed of the motor; the speed of the motor is not measured directly. The motor controller might commutate to early or to late due to an incorrect detection of the motor's orientation, especially at higher speed (refer to Fig. 10). As a result, and due to the relative slow dynamics of a motor, the commutation time consist of more high frequent signals, or peaks, than actual speed of the motor.

The calibration has been performed by both initializing the strain gauge measurement and F/T sensor force at zero. The gain has been determined by using the measured data from zero till 24 second. From 24 seconds till roughly 41 seconds the F/T sensor measures a large fluctuating force, which the strain gauge does not, or with a much lower amplitude, measure. Moreover, the vibrations cause an offset to occur in the F/T sensor's measurement, while no offset variations are present in the strain gauge's measurement. An FFT analysis has shown that the fluctuating force lies in the frequency range of 10 to 18 Hz. Experiments in which the F/T sensor was being hold by hand, i.e. less rigidity and more vibrational damping than a table, resulted in a significant reduction of the fluctuation's amplitude. Therefore, it is expected that the fluctuations in the F/T sensor's measured force are due to the interconnection of the F/T sensor and the table.

During the first part of the measurement (5 till 8 seconds) and the last part (60 till the end), fluctuation of the measured strain gauge data can be observed. These however coincides with the speed of the actuator; an FFT analysis has shown that the fluctuation consist of an vibration with exactly the same frequency as the motor is running.

Because of the large fluctuations in the measurements of the F/T sensor, its results are left out in the sequel.

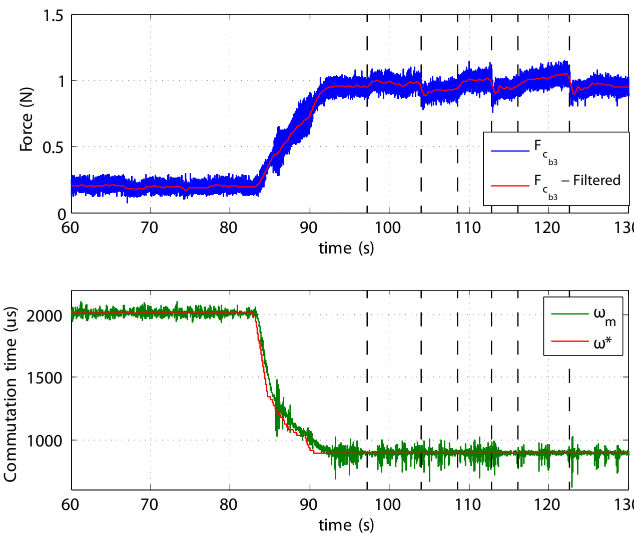

Fig. 11. Experiments 2: Influence of the ground effect on the force measured by the strain gauges. In the top plot the force measured by the strain gauge (blue) and its low pass filtered version are shown (red). In the bottom plot the measured commutation time of the motor (green) and the reference commutation time are shown (red).

In Fig. 11, the results of the second experiment are shown. During this experiment an large piece of paper is, at times, held below the multi-rotor's propeller at a distance of 60 mm. This paper represents represents the situation where the multi-rotor has to fly over an object. At each vertical line in the figure the piece of paper is either added or removed.

The theoretically predicted ground effect is clearly reflected in the measurements; adding a piece of paper results in a increase of average thrust increase of 7.8%, while removing it results in a (average) sudden thrust reduction of 12.4 %. This large reduction of thrust is expected to be due to the aerodynamics; the airflow requires time to recover.

During each section the thrust is regulated with a standard deviation of 3.1 % of the average value. From 95 second onwards the commutation time has a standard deviation of 3.8% of its average value, although higher order frequent signals are present in this measure as mentioned.

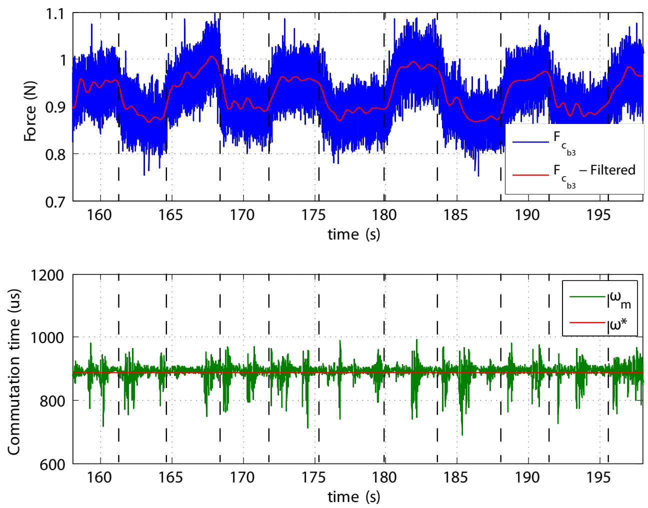

Fig. 12. Experiments 3: Influence of an neighboring wall on the force measured by the strain gauges. In the top plot the force measured by the strain gauge (blue) and its low pass filtered version are shown (red). In the bottom plot the measured commutation time of the motor (green) and the reference commutation time are shown (red).

In Figure 12, the results of the third experiments are shown. During this experiment, which is performed after the second experiment, a large piece of paper representing a wall is folded around the propeller at a distance of 10mm, with the center of the paper aligned with the propeller axis. Adding the wall decreases the thrust with an average of 9.2 %.

C. Evaluation

All subsystem of the multi-rotor have proven to be operational and are able to successfully perform their tasks. However, torsional vibrations created unreliable electrical connections. As a result, the multi-rotor hasn't made it first flight. These torsional vibration were detected during the design phase, but during that phase, the motors were not properly balanced which increased the induced vibrations. Furthermore, less induced vibration were expected during flight, as the multi-rotor becomes a floating mechanical system. Also, unreliable electrical connections were not detected.

The detection of the torsional vibration in the design phase has led to the design decision of making an option available to increase the torsional stiffness of the arms. This should lead to the attenuating of the induced vibrations. Moreover, not only can this option be used to stiffen the arms, it can also be used to reduce the stress on the components placed on the arms, thereby solving the unreliable electrical connections. In case, this does not solve the problem a redesign would be required. Components that are vulnerable to stress should in the redesign not be located on the arms.

From the first experiment it can be concluded that the setup in which the F/T sensor is mounted to a table is unsatisfactory. The F/T sensor measures large force fluctuations which seem not be present in the strain gauge's measurement. However, they could be present with a smaller amplitude and therefore an new setup is required in which this problem is tackled. A setup in which the F/T sensor is suspended by ropes between two tables should eliminate this problem. The ropes, namely have a low bending stiffness while they still provide a high axial stiffness to keep the setup in place.

Nonetheless from all three experiment it can be concluded that the strain gauge is able to successfully measure the thrust. Furthermore the ground effect and the effect of flying close to a wall are clearly reflected in the thrust measurements. These effects result in a variation of the thrust that lies in the range of 7.8 % till 12.4 % of the its actual value. It is therefore expected that a thrust controller is able to attenuate this effect and hereby improve the multi-rotor's performance.

VI. Conclusion

In this paper a new scheme is presented in which thrust sensors are used to control the thrust force of each individual actuator.

Analysis on the proposed scheme have been performed to determine its limitation. The analysis has shown that, not only the thrust force can be measured, but also the torques on the multi-rotor can be measured. These torque might be useful to improve the estimation of a multi-rotor's state, but further research is required to determine its effectiveness. During the analysis a mass ratio has been introduced that determines the effectiveness of the proposed scheme. Ideally the mass ratio should be infinity which is difficult to achieve with conventional multi-rotor designs. New ways of designing a multi-rotor with as criteria the mass ratio should therefore be investigated profoundly.

A new multi-rotor platform has been presented that incorporates thrust sensors. The multi-rotor platform does not only serve as platform to test the thrust sensors; the platform also serves as a new research platform. Its modular design gives the user the ability to add additional modules such as sensors or communication modules. Furthermore for image processing applications a Gumstix Overo, with an onboard DSP and additional cameras can be added to the multi-rotor.

All the subsystem of the multi-rotor have successfully been tested and perform their tasks reliably. However, due to torsional vibrations, induced by the motors, electrical connections on the multi-rotor's arm have proven to be unreliable. As a result, the multi-rotor has yet to make its first flight. This problem might however be easy to solve with the proposed modifications.

Furthermore, experiments have been performed to characterize the thrust sensors and these experiments showed promising results. It was shown that the influence of the ground effect and the effect of flying close to a wall can be measured by the thrust sensors. As the impact of these effect on the thrust is significant, it is expected that these effects can be successfully attenuated by the proposed thrust control scheme.

REFERENCES

[1] A. Kushleyev, D. Mellinger, C. Powers, and V. Kumar, "Towards a swarm of agile micro quadrotors," *Autonomous Robots*, vol. 35, no. 4, pp. 287–300, 2013.

[2] C. Lehnert and P. Corke, "μav - design and implementation of an open source micro quadrotor," in *Australasian Conference on Robotics and Automation (ACRA2013)* (J. Katupitiya, J. Guivant, and R. Eaton, eds.), (University of New South Wales, Sydney, NSW), pp. 1–8, Australian Robotics & Automation Association, 2013.

[3] R. Konomura and K. Hori, "Designing hardware and software systems toward very compact and fully autonomous quadrotors," in *Advanced Intelligent Mechatronics (AIM), 2013 IEEE/ASME International Conference on*, pp. 1367–1372, July 2013.

[4] S. Bouabdallah, P. Murrieri, and R. Siegwart, "Design and control of an indoor micro quadrotor," in *Robotics and Automation, 2004. Proceedings. ICRA '04. 2004 IEEE International Conference on*, vol. 5, pp. 4393–4398 Vol.5, April 2004.

[5] R. Mahony, V. Kumar, and P. Corke, "Multirotor aerial vehicles: Modeling, estimation, and control of quadrotor," *Robotics Automation Magazine, IEEE*, vol. 19, pp. 20–32, Sept 2012.

[6] C. Powers, D. Mellinger, A. Kushleyev, B. Kothmann, and V. Kumar, "Influence of aerodynamics and proximity effects in quadrotor flight," in *Experimental Robotics* (J. P. Desai, G. Dudek, O. Khatib, and V. Kumar, eds.), vol. 88 of *Springer Tracts in Advanced Robotics*, pp. 289–302, Springer International Publishing, 2013.

[7] P. Martin and E. Salaun, "The true role of accelerometer feedback in quadrotor control," in *Robotics and Automation (ICRA), 2010 IEEE International Conference on*, pp. 1623–1629, May 2010.

[8] M. Orsag and S. Bogdan, "Hybrid control of quadrotor," in *Control and Automation, 2009. MED '09. 17th Mediterranean Conference on*, pp. 1239–1244, June 2009.

[9] H. Huang, G. Hoffmann, S. Waslander, and C. Tomlin, "Aerodynamics and control of autonomous quadrotor helicopters in aggressive maneuvering," in *Robotics and Automation, 2009. ICRA '09. IEEE International Conference on*, pp. 3277–3282, May 2009.

[10] S. Lupashin, A. Schollig, M. Sherback, and R. D'Andrea, "A simple learning strategy for high-speed quadrocopter multi-flips," in *Robotics and Automation (ICRA), 2010 IEEE International Conference on*, pp. 1642–1648, May 2010.

[11] A. Awan, J. Park, and H. J. Kim, "Thrust estimation of quadrotor uav using adaptive observer," in *Control, Automation and Systems (ICCAS), 2011 11th International Conference on*, pp. 131–136, Oct 2011.

[12] H. Bangura, M.and Lim, H. J. Kim, and R. Mahony, "Aerodynamic power control for multirotor aerial vehicles," in *Robotics and Automation, 2014. ICRA '14. IEEE International Conference on*, pp. –, May 2014.

[13] E. Coelingh, T. J. A. De Vries, and R. Koster, "Assessment of mechatronic system performance at an early design stage," *Mechatronics, IEEE/ASME Transactions on*, vol. 7, pp. 269–279, Sep 2002.

[14] J. L. Scholten, "Phase 1: experimental results and multi-rotor design decisions." Attached as Appendix II.

[15] J. L. Scholten, "User Requirement Specifications (URS)." Attached as Appendix III.

[16] S. Madgwick, A. Harrison, and R. Vaidyanathan, "Estimation of imu and marg orientation using a gradient descent algorithm," in *Rehabilitation Robotics (ICORR), 2011 IEEE International Conference on*, pp. 1–7, June 2011.

[17] J. Chou, "Quaternion kinematic and dynamic differential equations," *Robotics and Automation, IEEE Transactions on*, vol. 8, pp. 53–64, Feb 1992.

[18] ATI Net F/T Sensor System. http://www.ati-ia.com/products/ft/ft_NetFT.aspx.

APPENDIX I
DERIVATION OF THE DYNAMIC EQUATIONS

For a multi-rotor with n actuators, and with the assumptions made in Section II the following holds (refer to Fig. 4):

$$m_b \cdot a_b = \sum_{i=1}^{i=n} F_{c_{bi}} + F_{dis} \tag{1}$$

$$m_x \cdot a_x = F_{Tx} - F_{c_{bx}} \tag{2}$$

In Laplace domain:

$$v_b = \frac{\sum_{i=1}^{i=n} F_{c_{bi}} + F_{dis}}{m_b \cdot s} \tag{3}$$

$$v_x = \frac{F_{Tx} - F_{c_{bx}}}{m_x \cdot s} \tag{4}$$

For $F_{c_{bx}}$ holds:

$$F_{c_{bx}} = \frac{1}{s} \cdot (v_x - v_b) \cdot c_{bx} \tag{5}$$

Using (3) and (4) results in:

$$\begin{aligned} F_{c_{bx}} = \frac{1}{s} \cdot \Big(& \frac{F_{Tx} - F_{c_{bx}}}{m_x \cdot s^2} \\ & - \frac{\sum_{i=1}^{i=n} F_{c_{bi}} + F_{dis}}{m_b \cdot s} \Big) \cdot c_{bx} \end{aligned} \tag{6}$$

$$\begin{aligned} & F_{c_{bx}} \left(1 + \frac{c_{bx}}{m_1 \cdot s^2} + \frac{c_{bx}}{m_b \cdot s^2}\right) = \\ & \qquad \frac{F_{c_{bx}} \cdot c_{bx}}{m_1 \cdot s^2} - \frac{\sum_{i!=x} F_{c_{bx}} + F_{dis}}{m_b \cdot s^2} \end{aligned} \tag{7}$$

$$\begin{aligned} F_{c_{bx}} = & \frac{\frac{c_{bx}}{m_x}}{s^2 + \frac{c_{bx}}{m_x} + \frac{c_{bx}}{m_b}} \cdot F_{Tx} \\ & - \frac{\frac{c_{bx}}{m_b}}{s^2 + \frac{c_{bx}}{m_x} + \frac{c_{bx}}{m_b}} \cdot (\sum_{i!=x} F_{c_{bx}} + F_{dis}) \end{aligned} \tag{8}$$

Introducing $H^{c_{bx}}_{F_{Tx}}$ and $H^{c_{bx}}_{F_{dis}}$:

$$H^{c_{bx}}_{F_{Tx}} = \frac{\frac{c_{bx}}{m_x}}{s^2 + \frac{c_{bx}}{m_x} + \frac{c_{bx}}{m_b}} \tag{9}$$

$$H^{c_{bx}}_{F_{dis}} = -\frac{\frac{c_{bx}}{m_b}}{s^2 + \frac{c_{bx}}{m_x} + \frac{c_{bx}}{m_b}} \tag{10}$$

which results in:

$$F_{c_{bx}} = H^{c_{bx}}_{F_{Tx}} \cdot F_{Tx} - H^{c_{bx}}_{F_{dis}} \cdot (\sum_{i!=x} F_{c_{bx}} + F_{dis}) \tag{11}$$

A. Two actuators and disturbance force

In case two actuators are present, e.g. actuator 1 and 3, the following is obtained:

$$F_{c_{b1}} = H^{c_{b1}}_{F_{T1}} \cdot F_{T1} - H^{c_{b1}}_{F_{dis}} \cdot (F_{c_{b3}} + F_{dis}) \tag{12}$$

$$F_{c_{b3}} = H^{c_{b3}}_{F_{T3}} \cdot F_{T3} - H^{c_{b3}}_{F_{dis}} \cdot (F_{c_{b1}} + F_{dis}) \tag{13}$$

Using (13) in (12) results in:

$$F_{c_{b1}} = H_{F_{T1}}^{C_{b1}} \cdot F_{T1} - H_{F_{dis}}^{C_{b1}} \cdot \Big(H_{F_{T3}}^{C_{b3}} \cdot F_{T3} - H_{F_{dis}}^{C_{b3}} \cdot (F_{c_{b1}} + F_{dis}) + F_{dis} \Big) \tag{14}$$

Moving $F_{c_{b1}}$ to the other size:

$$F_{c_{b1}}(1 - H_{F_{dis}}^{C_{b1}} \cdot H_{F_{dis}}^{C_{b3}}) = H_{F_{T1}}^{C_{b1}} \cdot F_{T1} - H_{F_{dis}}^{C_{b1}} \cdot \Big(H_{F_{T3}}^{C_{b3}} \cdot F_{T3} - H_{F_{dis}}^{C_{b3}} \cdot F_{dis} + F_{dis} \Big) \tag{15}$$

Rearranging on the right size:

$$F_{c_{b1}}(1 - H_{F_{dis}}^{C_{b1}} \cdot H_{F_{dis}}^{C_{b3}}) = H_{F_{T1}}^{C_{b1}} \cdot F_{T1} - H_{F_{dis}}^{C_{b1}} \cdot H_{F_{T3}}^{C_{b3}} \cdot F_{T3} + (H_{F_{dis}}^{C_{b1}} \cdot H_{F_{dis}}^{C_{b3}} - H_{F_{dis}}^{C_{b1}}) \cdot F_{dis} \tag{16}$$

And finally dividing both size by $(1 - H_{F_{dis}}^{C_{b1}} \cdot H_{F_{dis}}^{C_{b3}})$ results in:

$$F_{c_{b1}} = \frac{H_{F_{T1}}^{C_{b1}}}{1 - H_{F_{dis}}^{C_{b1}} \cdot H_{F_{dis}}^{C_{b3}}} \cdot F_{T1} - \frac{H_{F_{dis}}^{C_{b1}} \cdot H_{F_{T3}}^{C_{b3}}}{1 - H_{F_{dis}}^{C_{b1}} \cdot H_{F_{dis}}^{C_{b3}}} \cdot F_{T3} - \frac{H_{F_{dis}}^{C_{b1}} - H_{F_{dis}}^{C_{b1}} \cdot H_{F_{dis}}^{C_{b3}}}{(1 - H_{F_{dis}}^{C_{b1}} \cdot H_{F_{dis}}^{C_{b3}})} \cdot F_{dis} \tag{17}$$

To keep the naming convention correct, $H_{c_{b3}}^{F_{dis}}$ is introduced which equals 1:

$$F_{c_{b1}} = \frac{H_{F_{T1}}^{C_{b1}}}{1 - H_{F_{dis}}^{C_{b1}} \cdot H_{F_{dis}}^{C_{b3}}} \cdot F_{T1} - \frac{H_{F_{dis}}^{C_{b1}} \cdot H_{c_{b3}}^{F_{dis}} \cdot H_{F_{T3}}^{C_{b3}}}{1 - H_{F_{dis}}^{C_{b1}} \cdot H_{F_{dis}}^{C_{b3}}} \cdot F_{T3} - \frac{H_{F_{dis}}^{C_{b1}} - H_{F_{dis}}^{C_{b1}} \cdot H_{F_{dis}}^{C_{b3}}}{(1 - H_{F_{dis}}^{C_{b1}} \cdot H_{F_{dis}}^{C_{b3}})} \cdot F_{dis} \tag{18}$$

Or in terms of sensitivity:

$$F_{c_{b1}} = S_{F_{T1}} \cdot F_{T1} - S_{F_{dis}} \cdot F_{dis} - S_{F_{T3}} \cdot F_{T3} \tag{19}$$

$$S_{F_{T1}} = \frac{H_{F_{T1}}^{C_{b1}}}{1 - H_{F_{dis}}^{C_{b1}} \cdot H_{F_{dis}}^{C_{b3}}} \tag{20}$$

$$S_{F_{dis}} = \frac{H_{F_{dis}}^{C_{b1}} \cdot H_{c_{b3}}^{F_{dis}} \cdot H_{F_{T3}}^{C_{b3}}}{1 - H_{F_{dis}}^{C_{b1}}} \tag{21}$$

$$S_{F_{T3}} = \frac{H_{F_{dis}}^{C_{b1}} - H_{F_{dis}}^{C_{b1}} \cdot H_{F_{dis}}^{C_{b3}}}{(1 - H_{F_{dis}}^{C_{b1}} \cdot H_{F_{dis}}^{C_{b3}})} \tag{22}$$

$$H_{c_{b3}}^{F_{dis}} = 1 \tag{23}$$

B. Four actuators and disturbance force

For four actuators equation (11) still is valid. However the derivation becomes much more complex and therefore symbolic analysis in MATLAB has been used to determine the transfer functions and relations introduced. The used MATLAB script can be downloaded from: `https://www.dropbox.com/s/jakfv2nsm1srb7f/DerivationOfTheDynamicEquations.m?dl=0`

Appendix II:

Phase 1: experimental results and multi-rotor design decisions

Rev. 1.0

ROBOTICS
AND
MECHATRONICS

Jasper L.J. Scholten BSc
Supervisors: Prof. Stefano Stramagioli, Dr. ir. Theo J.A. de Vries,
Dr. Matteo Fumagalli

October 17, 2014

UNIVERSITY OF TWENTE.

Contents

Chapter 1

Introduction

1.1 Context

Within the Robotics and Mechatronics research group at the University of Twente, there is need for a new multi-rotor research platform. Instead of buying one, it has been decided to develop a multi-rotor platform which is able to satisfy all requirement while at the same time integrating a novelty: integrated thrust sensors to improve the multi-rotor's performance.
In order to decide on the dimensions of the multi-rotor, in a first iteration several variants, with different sized propellers and motors, have been developed on paper. For these variants assumptions about the thrust generated by each combination of motor and propeller have been made. This is due to the fact that limited information is available for the small sized (hobby) motors and (hobby) propellers considered.
To make a profound choice on the design of the multi-rotor, experiments have been performed. These experiments have been performed on a developed test bed, that enabled the characterisation of several motor and propeller combinations. At the same time the test bed was meant to be used to verify the developed integrated thrust sensors in a static (non flying) environment, but these results are not included yet.

1.2 Purpose

In this report the results and the corresponding conclusions of the performed experiments are discussed.
This document supports the following objectives:

- Document the physical parameters of the motors and propellers used.
- Document the measurement results of each motor and propeller combination.
- Document the accuracy of the measurements.
- Identify the alternatives
- Identify the weighing criteria
- Decision on multi-rotor design.

1.3 References

Applicable references are:

1. Test Plan - Iteration 1 - 16/04/2014
2. Feasibility study - 13/03/2014
3. User Requirement Specification (URS) - 10/03/2014
4. Work Breakdown Structure (WBS) v2 - 12/04/2014
5. Project Plan - 10/03/2014

Chapter 2

Measurement results

2.1 Physical parameters

In Table 2.1 the physical parameters, such as mass, resistance and inductance, of each motor and where applicable the parameters of propeller are listed. The mass is measured with an JS-100xV scale that has an accuracy of ±0.01 $[g]$. The resistance and inductance are measured at a frequency of 1 $[kHz]$ with an HM8118 LCR Bridge HAMEG at a test voltage of 1 $[V]$.

Motor	**mass** ±0.01 **[g]**	**R** $[m\Omega]$	**L @ 1kHz** $[\mu H]$
AP02 7000Kv	2.40	389.3±3.5	19.3±0.3
AP03 4000Kv	3.19	505±1.0	31.2±0.6
A1309-7500Kv	3.13	307±4.7	14.2±0.7
1404N 2290Kv	8.11	411.8±2.0	30.3±3.9
C05M 11000Kv	4.10	154.6±1.3	4.6±0.6
S5 13000Kv	3.98	88.4±0.8	2.8±0.3
C05XL 10800Kv	6.81	65.1±0.4	1.8±0.2
2508 propeller	0.44	-	-
3020 propeller	1.35	-	-
4020 propeller	1.43	-	-

Table 2.1: Physical parameters of motors and propellers

2.2 Static experiments

In Table 2.2 for each motor and propeller combination tested, several results are shown. These are the maximum thrust for a given voltage, the power consumption at maximum thrust, the thrust to mass ratio and thrust to power ratio. The thrust has been indirectly measured with an 6 DOF force and torque sensor from ATI (Mini40E). During all experiments the commercial Electronic Speed Controller (ESC) was used. For a complete overview of the test setup, please refer to Test Plan - Iteration 1 - 16/04/2014.

The torque measured is used to compute the thrust in grams with the following equation:

$$T = \tau_m \cdot \frac{1}{l_{arm}} \cdot A_{NtoGram}[g] \tag{2.1}$$

with l_{arm} being equal to the distance between the axis of the motor and the center of the transducer (75$[mm]$). $A_{NtoGram}$ is equal to $1000/g$, where g is the standard acceleration of gravity(9.80665 $[m/s^2]$). In Figure 2.1 the thrust as function of time is shown for one motor and propeller combination to illustrate the measurement data acquired.
The power versus thrust curve of each motor propeller combination is added as attachement to this report.

For each motor and propeller combination a curve has been fitted to the acquired data. In Figure 2.2, for the motor and propellers combination for which a power curve could be fitted, the result is shown. In most cases 5 different thrust levels are used to fit a curve. However for

Motor & propeller	**Voltage** $[V]$	$T_m \pm 1$ $[g]$	$P_m \pm 2.2\%$ $[W]$	$\frac{T_m}{P_m}$	$\frac{T_m}{m}$
AP02 7000kV	-	-	-	-	0
AP03 4000kV & 2508	7.74	25.0	11.6	2.16	6.89
AP03 4000kV & 3020	7.74	40.2	15.2	2.64	8.85
AP03 4000kV & 4020	7.74	47.1	15.2	3.10	10.19
A1309 7500kV & 2508	7.74	18.6	25.4	0.73	5.21
A1309 7500kV & 3020	7.74	54.8	23.2	2.36	12.23
A1309 7500kV & 4020	7.74	56.4	24.5	2.30	12.37
1404N 2290kV & 3020	7.74	46.6	7.4	**6.30**	4.93
1404N 2290kV & 3020	11.10	85.4	17.7	4.83	9.03
1404N 2290kV & 4020	7.74	72.7	12.3	5.91	7.62
1404N 2290kV & 4020	11.10	121.4	28.5	4.26	**12.73**
C05M 11000kV	7.74	43.3	33.3	1.33	10.56
S5 13000kV & 2508	7.74	43.8	23.2	1.89	9.91
S5 13000kV & 3020	7.74	31	23.2	1.34	5.82
C05XL 10800kV & 3020	7.74	46.6	23.2	2.01	5.71

Table 2.2: Measurement results of all motor and propeller combinations. AP02 wouldn't start while both S5 and C05XL reached a too high current and thus the maximum voltage (PWM) has not been applied.

C05M only two are used as it wasn't able to start well with a propeller attached. If this was due to an defect motor is unknown. For both the S5 and C05XL also two levels are used as the current was becoming too high (inefficient and reaching maximum allowed current).

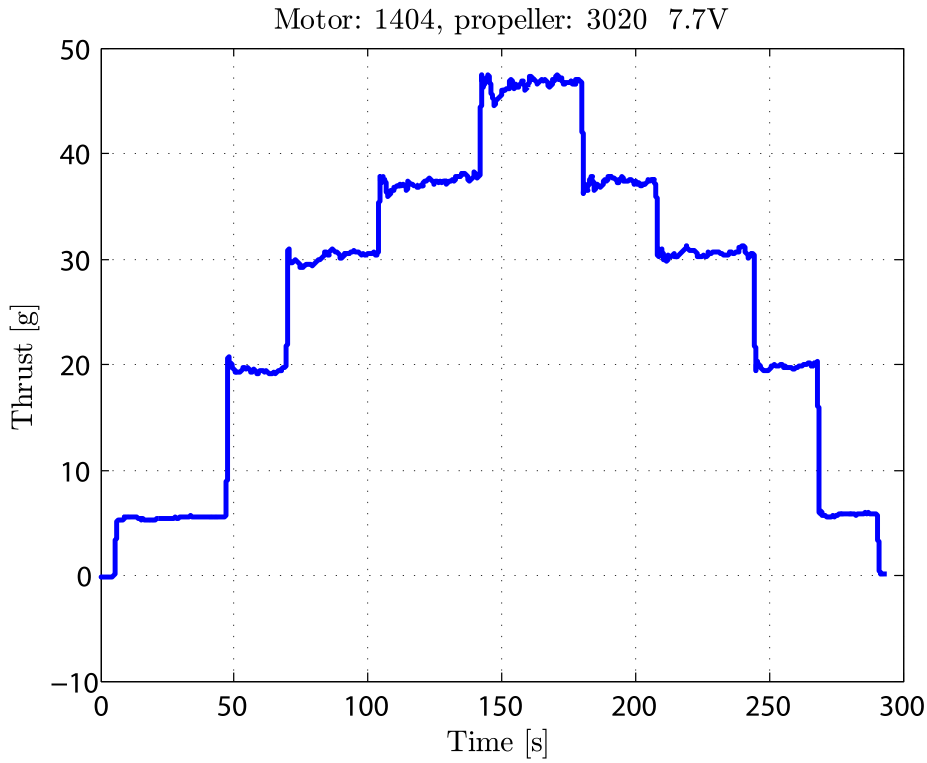

Figure 2.1: Measurement data of one motor and propeller combination. Illustrating the measurement method used.

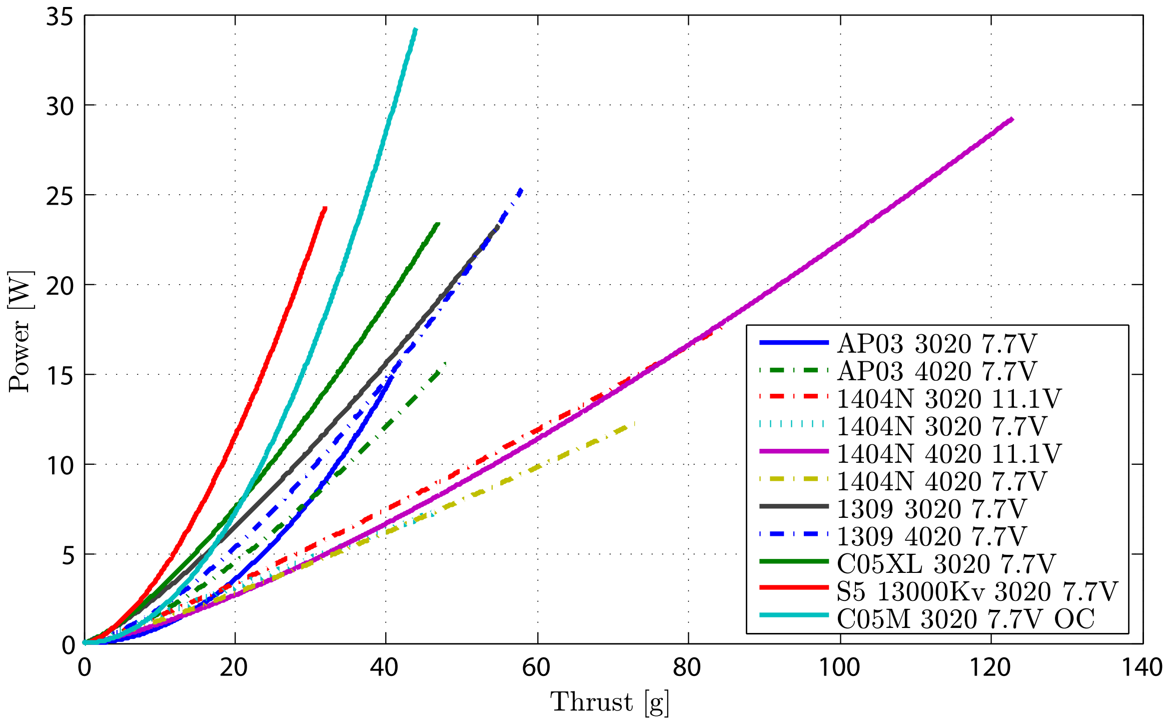

Figure 2.2: Power versus thrust fit of each motor and propeller combination

2.3 Step response

In Figure 2.3 a step response of the 1404N and AP03 motor is shown. For the step response of the 1404N motor System Identification Toolbox is used to estimate the transfer function. A 4th order transfer function was fitted which has the best fit of 96.44 %.:

$$\frac{Thrust}{voltage} = \frac{1528}{s^4 + 6.569s^3 + 42.61s^2 + 129.2s + 198.2} \tag{2.2}$$

$$p1 \ \& \ p2 : -1.06 \pm 4.92i \tag{2.3}$$

$$p3 \ \& \ p4 : -2.22 \pm 1.70i \tag{2.4}$$

Note: a 5 Hz low pass filter in the force/torque sensor was applied.

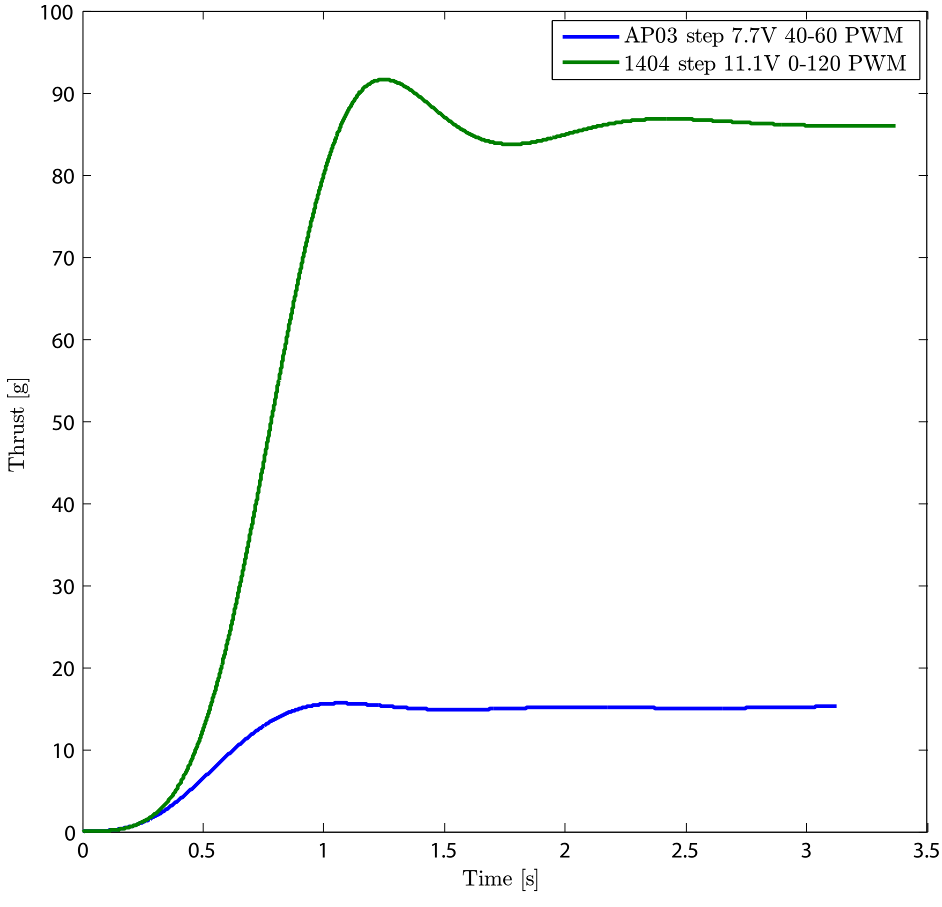

Figure 2.3: Step response of 1404N motor from standstill to full throttle and of AP03 from 1/3 to 1/2 throttle.

2.4 Measurement accuracy

2.4.1 Thrust

The resolution of the ATI Mini40E transducer is specified as 1/4000 $[Nm]$, while for accuracy of the torque measurements only the typical gain error over temperature (deviation from 22°C) is specified:

- $\pm 5°C$: 0.1%
- $\pm 15°C$: 0.5%

The analog signal is digitalised by a 16bits ADC in the NET F/T box of ATI that enables it to be interfaced via Ethernet. Also the NET F/T box is used to apply a 5 Hz digital low pass first order filter as for the measurement results in Table 2.2 only the low frequent component is necessary.
Assuming l_{arm} and $A_{NtoGram}$ are correct, given the typical gain error and equation 2.1, the thrust has an typical error of 0.1 %. However, as can be seen in Figure 2.1, the thrust varies over time with roughly $\pm 1[g]$.

2.4.2 Power

During each step in Figure 2.1 the DC current was measurement with a Fluke 175 True RMS multimeter which has an specified accuracy of ±1% [Fluke(2001)]. During measurement, especially when the motors were spinning at a high RPM, the DC current fluctuated with roughly ±2% max. The voltage was measured with the same Fluke 175 multimeter. The multimeter has an voltage measurement accuracy of 0.15%. Given the fact a relative light load is applied to the 300 $[W]$ power supply and by measuring the voltage under load, it was concluded that the effect of an varying voltage on the power consumption can be neglected. Assuming the uncertainties are uncorrelated the maximum deviation in computed power becomes 2.2 %.

Please note that the computed power is also due to the losses that occur in the motor controller. The power consumption due to the idle current (motor not running) has been found to be negligible (0.1 [W]).

Chapter 3

Multi-rotor alternatives

In this section the multi-rotor alternatives discussed and weighed using a weighing matrix. In order to make a profound choice, the criteria need to be determined. These criteria originate from the user requirement and the results from the feasibility study. After the introduction of the alternatives the these criteria are determined after which they are applied in a weighing matrix in Section 3.4.

3.1 Alternatives

From the results of Chapter 2, eight alternative configurations have been composed. These are shown in Figure 3.1. Four alternatives use the 3020 propeller, while the other four use the 4025 propeller. This difference is expressed in the naming: 107-XX-XX respectively 127-XX-XX. The second part of the name list the number of battery cells it operates on. The 2S variant uses a two cell battery while the 3S variant uses a three cell battery. The voltage respectively is 7.4 $[V]$ and 11.1 $[V]$. The last difference is the motor that is being used. LP stands for an motor with a low power consumption, but has other disadvantages such as size and weight. MP stands uses a motor with medium power consumption while HP stands uses motor with an high power usage. To conclude, each alternative uses an different class motor, each with its own disadvantages and advantages.
The flight time is calculated when everything is running at full power and in case a gumstix and two cameras used. The hover time is also calculated in case a gumstix and two cameras are used. The thrust to mass ratio is defined as the maximum thrust divided by the mass of the multi-rotor *without* payload. Thus without gumstix, camera etc. The mass is again the mass of the multi-rotor without payload. The mass ratio R_m is also defined for the case without payload.
Several comments need to be made about the component choices:

- Reducing flight time, by reducing the size of battery, also reduces Rm, but does increase the thrust to mass ratio and the payload.
- If an high R_m isn't necessary, reducing battery size and thus flight time, significatly increases the thrust to mass ratio.

Power consumption using 2S (7.4V bat)

.	107-2S-LP (Low)	107-2S-MP (Medium)	107-2S-HP (High)
Size (mm)	107x107	107x107	107x107
Flight time (min)	6.2	6.7	5.6
Hover time (min)	9.8	14.9	11.5
T/m	2.0	1.7	2.1
mass (g)	93.8	94.2	102.9
Payload T/m=2	-1.6	-14.8	5.7
Payload T/m=1	91.6	65.6	115.3
Rm	5.9	16.7	19.0

Using 3S (11.1V battery)

.	107-3S
Size (mm)	107x107
Flight time (min)	8.6
Hover time (min)	19.5
T/m	2.5
mass_empty (g)	136.8
Payload T/m=2	33.0
Payload T/m=1	203.8
Rm	10.5

.	127-2S-LP	127-2S-MP	127-2S-HP
Size (mm)	127x127	127x127	127x127
Flight time (min)	8.2	6.0	5.3
Hover time (min)	17.3	11.0	12.0
T/m	2.3	1.6	2.0
mass (g)	124.2	102.5	113.2
Payload T/m=2	20.2	-23.1	-1.4
Payload T/m=1	165.6	57.3	111.4
Rm	9.0	18.2	20.8

.	127-3S
Size (mm)	127x127
Flight time (min)	10.3
Hover time (min)	25.8
T/m	2.3
mass (g)	210.2
Payload T/m=2	31.6
Payload T/m=1	274.4
Rm	18.0

Figure 3.1: Multirotor alternatives. Highlighted in red the best score of each size (107 and 127). Highlighted in black the best score overall.

3.2 Derivation of weighing criteria

3.2.1 User requirement specifications

In order to determine which motor and propeller, and thus the dimensions of the multi-rotor, should be used, it is necessary to review associated user requirements. These requirements are listed in Table 3.1. Requirement H.PR.04 has been updated to include a necessary hover time of 10 minutes.

Reference	Item	Description	Priority (N/D/O)
H.GR.04	Dimensions	The size of the multi-rotor should be as small as possible, where the exact size is still to be determined. Necessary is that the size is smaller than 300 [mm] x 300 [mm] such that multiple multi-rotors can be employed in the flying facility at the RAM chair.	N

H.PR.02	Maneuverability	The maneuverability of an multi-rotor can be expressed as the ratio of available thrust and of the weight of the aircraft. The following is required and desired, given the fact acrobatic movements are required to be made: • $\frac{m_{thrust}}{m_{weight}} = 2$ • $\frac{m_{thrust}}{m_{weight}} = 4$	• N • D
H.PR.04	Flight/Hover time	A flight time of 10 minutes, computed with maximum power consumption is desired. Necessary is an hover timer of 10 minutes.	D

Table 3.1: Associated requirements to decide on motor and propeller combination

3.2.2 Payload

Other then size, maneuverability and flight/hover time, the payload is important. The payload is defined as the extra mass the multi-rotor is able to carry; e.g. extra sensors, cameras etc. Several user requirements are listed in the URS document which have a direct impact on the required payload capacity. These mainly are:

- Usage of a gumstix
- Two camera capability
- Altitude control --→ height measurement
- Opti-track compatibility
- Indoor/outdoor localisation
- Wireless communication

The estimated weight of the components necessary for each item has been listed in Table 3.2.

Item	mass [g]
Gumstix Overo	5.6
Gumstix Antenna 2x	11.8
Sonar MaxBotic	4.3
Camera	
- High quality gumstix compatilble Caspa VL	22.9
- Nano	2.7
Indoor/outdoor localisation	10
Wireless communication	
- Bluetooth & Wifi included on Gumstix	-
- Bluetooth chip	3

Table 3.2: Payload determining items

In case two nano cameras are used the payload required is 39.1 grams. In case two high quality cameras are used the payload requirement is 79.5 grams. However it should be noted that ideally, given these payload requirements, a thrust to mass ratio of 2 with this payload onboard is still desired (H.PR.02). The desired payload can thus be written as the mass of the multi-rotor plus the aforementioned payload.

3.2.3 Mass ratio

Note (17-10-2014): this section has been removed as it is not longer up-to-date. Please refer to the Master Thesis Report (Section II) for the latest findings.
R_m is added to the list of requirements to determine the best motor and propeller combination.

3.3 Weighing criteria

The requirements listed in the previous sections are now converted to criteria which can then be used to evaluate each multi-rotor alternative. The criteria are listed in Table 3.3. For each criteria it's possible to receive a predefined number of points, weighted on importance. The total number of points equals 100. The mass ratio has been given the highest priority as it is the biggest novelty of the to be developed multi-rotor.

Alternative \ **Criteria**	**(1)**	**(2)**	**(3)**	**(4)**	**(5)**	**(6)**	**Total**
107-2S-LP	2	5	4	11	6	0	28
107-2S-MP	8	3	3	11	6	4	35
107-2S-HP	9	5	5	11	5	1	36
107-3S	5	7	10	11	8	9	50
127-2S-LP	4	6	8	7	8	7	40
127-2S-MP	9	3	2	7	6	1	28
127-2S-HP	10	5	5	7	5	2	34
127-3S	9	6	13	7	10	10	55

Table 3.4: Weighing matrix for multi-rotor alternatives.

Criteria	**Points**	Explanation
(1) Rm	For each point, 0.5 points Max number of points: **30**	Twice as important as other requirements.
(2) Thrust to mass ratio	$\frac{T}{m} = 1 \Rightarrow 0$ points For each increase of 0.2 , 1 point Max number of points: **15**	30 points are given in case the thrust to mass ratio equals the max desired ratio of 4.
(3) Payload	For each 20 grams, 1 point Max number of points: **15**	A high (2) doesn't necessarily imply a high payload.
(4) Dimensions	300 $[mm]$ x 300 $[mm]$ = 0 points For each reduction of 10 $[mm]$, 1 point Max number of points: **15**	Smaller than 300x300 $[mm]$ is necessary. No extra points if smaller than 150x150 $[mm]$.
(5) Flight time	For each minute, 1 point Max number of points: **15**	Above 15 minutes the flight time becomes less important.
(6) Hover time	For each minute above 10 minutes, 1 point Max number of points: **10**	Above 20 minutes it becomes irrelevant.

Table 3.3: Criteria for evaluating multi-rotor alternatives, ranked by importance. Do not confuse (2) with (3) and visa versa.

3.4 Weighing matrix

Note (17-10-2014): the mass ratio used for the alternatives only takes the mass and not the inertia into account. Nonetheless, it leads to the same conclusion

In Table 3.4 the weighing matrix is shown. From this matrix it can be concluded that the winning alternative is the 127-3S with 55 points, followed with a small difference of 5 points by alternative 107-3S. The other alternatives follow at a rather large distance (15 - 27 points).

Chapter 4

Conclusion

In this report the first results of the first experimental phase have been discussed. Several motor and propeller combinations have been characterised. From these results eight multi-rotor alternatives have been composed. These alternatives have been held against six weighing criteria, which were derived from the user requirements and the feasibility study. One multi-rotor design, the 127-3S, outperforms all others by getting 55% of the total number of available points. The runner up got 50% while the others are around 28% to 40%. Given the fact the 127-3S achieved the highest score it is recommended to use this design.

Bibliography

[Fluke(2001)] Fluke. Calibration Information Fluke 175,177,&179 @ONLINE, March 2001. URL http://media.fluke.com/documents/17x_____cieng0500.pdf.

Appendix III:

User Requirement Specifications (URS)

Rev 1.0

Jasper L.J. Scholten BSc
Supervisors: Prof. Stefano Stramagioli, Dr. ir. Theo J.A. de Vries,
Dr. Matteo Fumagalli

October 17, 2014

UNIVERSITY OF TWENTE.

Contents

Chapter 1

Introduction

1.1 Purpose

In this report the user requirement specifications are discussed which define the purpose of the to be developed multi-rotor platform with integrated thrust sensors. The functions that need to be carried out, the required accuracy that needs to be achieved, the hardware on which the system will operate and the operating environment are identified. Furthermore also constrains are identified, such as costs, time and the deliverables.

1.2 Origin and context

Within the Robotics and Mechatronics research group at the University of Twente, there is need for a new multi-rotor research platform. Instead of buying one, it has been decided to develop a multi-rotor platform which is able to satisfy all requirement while at the same time integrating a novelty: integrated thrust sensors to improve the multi-rotor's performance.
A feasibility study has been done to determine the feasibility of using strain gauge sensors to measure the thrust. This study has been reported in the document "Development of a multi-rotor platform with integrated thrust sensors - Feasibility study".

1.3 Scope

This document defines the requirements for:

- Hardware platform
  - general
  - performance
  - interface
- Software platform
  - general
  - performance
  - interface

1.4 Document organisation

This document has the following sections:

#	Section	Sub-Section	Contains
2	Overview	Project summary	Short summary of what the project is part of.
		Key objective	Description of the key objectives of the project
		Main system functions	The main functions the system should provide.

3	Operational requirements	Hardware requirements	General hardware requirements, hardware performance and hardware interface requirements.
		Software requirements	General software requirements, software performance and software interface requirements.
4	Constrains	-	Constrains in costs, schedule, maintenance and deliverables.

Table 1.1: Document organisation

Chapter 2

Overview

2.1 Project overview

The development of the multi-rotor platform with integrated thrust sensors is the author's master thesis. The research is performed within the University of Twente at the Robotics and Mechatronics research chair. Furthermore the master thesis is part of the master program Electrical Engineering.

2.2 Key objectives

The key objective of this project is to realise the novelty of integrating thrust sensors in a multi-rotor in order to improve its performance, while at the same time developing a new research platform for the Robotics and Mechatronics chair.

2.3 Main system functions

The multi-rotor platform has to provide the following main functions:

- Provide increased observability and improved controllability for multi-rotors opposed to multi-rotor without thrust sensors; also proving the concept of integrated thrust sensors.
- Provide a research platform for the Robotics and Mechatronics laboratory of the University of Twente, such that research projects can be carried out which include multiple multi-rotors flying in formation, interaction with the environment, testing control laws etcetera.

Chapter 3

Operational requirements

The two general function of the multi-rotor platform given in the previous chapter can be converted to operational requirements. These in turn can be divided into hardware and software requirements. Each requirement is given a priority, which can be:

- Necessary (N): it has to be implemented in order for the project to be successful.
- Desired (D): if it's easy to implement then it should be.
- Optional (O): only implement it in case all other requirements are met and time is left.

3.1 Hardware requirements

The hardware requirements can be split into general hardware requirements, performance hardware requirements and interface requirements.

3.1.1 General hardware requirements

The general hardware requirements are discussed in Table 3.1.

Reference	**Item**	**Description**	**Priority (N/D/O)**
H.GR.01	Integrated thrust sensors	In order to measure the thrust generated by each of the multi-rotor motors, integrated thrust sensors are required. This is the concept which should be investigated and thus is a necessary requirement.	N
H.GR.02	Usage of gumstix [1]	As processing unit a gumstix should be used, as these are compact, powerful and have been used before within the RaM chair.	N
H.GR.03	Single Printed Circuit Board (PCB)	The frame of the multi-rotor should only consist of a single PCB; i.e. no external frame. Furthermore all the electronics should be integrated on this PCB.	N
H.GR.04	Dimensions	The size of the multi-rotor should be as small as possible, where the exact size is still to be determined. Necessary is that the size is smaller than 300 [mm] x 300 [mm] such that multiple multi-rotors can be employed in the flying facility at the RaM chair.	N
H.GR.05	Two camera capability	For later research projects, the multi-rotor should be able to carry two camera; one aiming forward and one aiming downwards. These can then be used for, for example, object recognition, localisation or inspection.	N

H.GR.06	Altitude control	To autonomously control the altitude of the multi-rotor with respect to the ground, an estimate is required. Altitude control can be used for both indoor and outdoor environments. For indoor this typically means a height of a few meter, while for outdoor operation this height can reach several tens of meters.	N
H.GR.07	Attitude control	To autonomously control the attitude of a multi-rotor these state of the multi-rotor should be estimated. This is done by using an N degree of freedom IMU, where N is often 6 or 9.	N
H.GR.08	Opti-track compatibility	In the laboratory of RaM there is a Vicon Motion capturing system to sense the position of (moving) targets. The multi-rotor should be compatible with this system such that it can be used for research projects.	N
H.GR.09	Outdoor localisation	In later research project outdoor localisation can be desired. It is thus required to estimated the position of the multi-rotor. Given the fact most projects will be indoor, this requirement has been given the desired (D) priority.	D
H.GR.10	Indoor localisation	For some application it can be desired to know the indoor position of the multi-rotor with respect to it's surrounding. An example application is obstacle detection, or SLAM. This requirement has been given the desired (D) priority as the others have an higher expectancy to be used.	D
H.GR.11	Battery exchange	One of the problems of battery powered multi-rotor systems is that the battery needs to be recharged or exchanged before they can continue their mission once the battery runs out. By creating the option of exchanging the battery in mid air, this problem can be eliminated. The same reasoning as in H.GR.1.0 is followed to assign the desired (D) priority to this requirement.	D

Table 3.1: General hardware requirements

3.1.2 Hardware performance requirements

The hardware performance requirements are discussed in Table 3.2.

Reference	Item	Description	Priority (N/D/O)
H.PR.01	Controller bandwidth	A control bandwidth is required which allows the multi-rotor to perform acrobatic movements such as flips. In [2] a flip is performed in 0.4 [s]. Given a desired tracking accuracy during a flip of 1 degree and a period of 0.4 [s], for a moving mass using a PID controller, this yields a required bandwidth of 22,5 [Hz] for a skew sine reference. This control bandwidth is assumed to be necessary for the to be developed multi-rotor. Subsystems of the multi-rotor system should comply with this control bandwidth.	N
H.PR.02	Maneuverability	The maneuverability of an multi-rotor can be expressed as the ratio of available thrust and of the weight of the aircraft. The following is required and desired, given the fact acrobatic movements are required to be made: • $\frac{m_{thrust}}{m_{weight}} = 2$ • $\frac{m_{thrust}}{m_{weight}} = 4$	• N • D
H.PR.03	Accuracy thrust measurement	In order to successfully improve the controllability of a multi-rotor with the thrust sensors, it is estimated that the following accuracy is required and desired: • $e_{max}(2\sigma) = 5$ % • $e_{max}(2\sigma) = 1$ %	• N • D
H.PR.04	Flight time	A flight time of 10 minutes is desired, but the necessary flight time is yet to be determined.	D

Table 3.2: Hardware performance requirements

3.1.3 Hardware interface requirements

The hardware interface requirements are discussed in Table 3.3.

Reference	Item	Description	Priority (N/D/O)
H.IR.01	Wireless communication	The multi-rotor should have an on-board wireless communication such that it can be controlled wirelessly.	N

H.IR.02	Firmware updates	The firmware of the processor(s) on the multi-rotor has to be updateable. This will require an interface.	N
H.IR.03	Docking station	In order to charge the battery of the multi-rotor a docking station can be created in later research projects. The multi-rotor should thus have an interface to charge its battery without having to remove the battery. This requirement has been given the desired (D) priority as the others have an higher expectancy to be used.	D

Table 3.3: Hardware interface requirements

3.2 Software requirements

The software requirements can be split into general software requirements, performance software requirements and interface requirements.

3.2.1 General software requirements

The general software requirements are discussed in Table 3.4.

Reference	**Item**	**Description**	**Priority (N/D/O)**
S.GR.01	Operating system	As operating system ROS is preferred due to the knowledge of ROS within the RaM group. This is thus given a desired (D) priority.	D

Table 3.4: General software requirements

3.2.2 Software performance requirements

The software performance requirements are discussed in Table 3.5.

Reference	**Item**	**Description**	**Priority (N/D/O)**
S.PR.01	Real time control	Given the fact that the low level control of a multi-rotor is time critical, a real time controller is desired (D).	D

Table 3.5: Software performance requirements

3.2.3 Software interface requirements

The software interface requirements are discussed in Table 3.6.

Reference	Item	Description	Priority (N/D/O)
S.IR.01	User interface	In order to control the multi-rotor a high level controller with an user interface has to be made.	N

Table 3.6: Software interface requirements

Chapter 4

Constrains

The constrains listed in Table 4.1 have to be met.

Reference	Item	Description	Priority (N/D/O)
C.0.1	Costs	The maximum costs of the project is yet to be determined.	N
C.0.2	Schedule	The maximum time given for this project is equal to 40 European Credits, or 1120 hours.	N
C.0.3	Maintenance	Maintenance to the multi-rotor have to be doable with the laboratory of RaM. Thus with standard electrical engineering equipment you can expect at an university.	N
C.0.4	Delivarables	At the end of the project a multi-rotor platform is presented, a master thesis report will be handed in and a presentation will be held for the members of RaM.	N

Table 4.1: Constrains

Bibliography

[1] Gumstix Overo. https://www.gumstix.com/. Accessed: 2014-01-29.

[2] A. Kushleyev, D. Mellinger, C. Powers, and V. Kumar. Towards a swarm of agile micro quadrotors. *Autonomous Robots*, 35(4):287–300, 2013.